

Cite this: *J. Mater. Chem. C*, 2018, **6**, 1780

## Effect of annealing temperature on the phase transition, band gap and thermoelectric properties of $\text{Cu}_2\text{SnSe}_3$ †

Muhammad Siyar,<sup>a</sup> Jun-Young Cho,<sup>a</sup> Yong Youn,<sup>a</sup> Seungwu Han,<sup>a</sup> Miyoung Kim,<sup>a</sup> Sung-Hwan Bae<sup>b</sup> and Chan Park<sup>c,\*ad</sup>

The effect of annealing temperature on the phase transition of  $\text{Cu}_2\text{SnSe}_3$  was investigated in order to study the thermoelectric (TE) properties of the various  $\text{Cu}_2\text{SnSe}_3$  phases. The stoichiometric composition of  $\text{Cu}_2\text{SnSe}_3$  was synthesized by melt solidification and annealing at various temperatures followed by water quenching. Rietveld refinement was used to calculate the amount of monoclinic and cubic phases for each sample. XRD analyses reveal that the samples annealed at 720 and 820 K have mostly a monoclinic phase along with a small amount of cubic phase. The  $\text{Cu}_2\text{SnSe}_3$  annealed at 960 K was mostly cubic. TE properties of the cubic phase  $\text{Cu}_2\text{SnSe}_3$  were studied for the first time, and it was found that it has much higher  $ZT$  ( $\sim 0.09$ ) than the monoclinic phase at 600 K. Better TE performance of the cubic phase can be attributed to the smaller band gap ( $\sim 0.92$  eV) compared to that of monoclinic  $\text{Cu}_2\text{SnSe}_3$  ( $\sim 1.0$  eV) at room temperature. First principles calculations further confirmed the conductive metallic nature of the cubic phase  $\text{Cu}_2\text{SnSe}_3$ . The power factor ( $S^2\sigma$ ) of the cubic phase,  $0.24 \text{ mW m}^{-1} \text{ K}^{-2}$ , was higher than that of the monoclinic phase,  $0.096 \text{ mW m}^{-1} \text{ K}^{-2}$ , at 600 K, but the difference between the thermal conductivities of the two phases was very small. Small polymorphic modification with increasing annealing temperature results in compositionally similar but different crystallographic phases, which is one of the possible reasons for the very similar thermal conductivities of the two phases. The electrical conductivity of the cubic phase, which is larger than that of the monoclinic phase, and the similar thermal conductivities of the two phases lead to the higher  $ZT$  of the cubic  $\text{Cu}_2\text{SnSe}_3$ .

Received 14th November 2017,  
Accepted 12th January 2018

DOI: 10.1039/c7tc05180h

rsc.li/materials-c

## Introduction

TE energy harvesting is one of the approaches being used to address the global environmental challenges, utilizing waste heat for useful electric power generation. This technology recently attracted the attention of the commercial sectors, due to the possible applications of TE materials in wearable electronic devices, solid-state Peltier cooling, remote area sensors, *etc.*<sup>1–3</sup> Currently available commercial TE materials such as  $\text{Bi}_2\text{Te}_3$ ,  $\text{Sb}_2\text{Te}_3$  and  $\text{PbTe}$  consist of either toxic or expensive elements.<sup>4,5</sup> Therefore, exploration of TE materials with less toxic, less expensive and more earth-abundant elements is the focus of

the TE community these days. The ternary chalcogenide  $\text{Cu}_2\text{SnSe}_3$  is expected to be one of these auspicious TE materials, having large flexibility to tune its physical and electronic properties.<sup>6</sup> The elements of  $\text{Cu}_2\text{SnSe}_3$  are less toxic, abundant in nature and relatively cheap compared to Te and Pb.

In the structure of  $\text{Cu}_2\text{SnSe}_3$ , Sn orbitals have a small effect on carrier transport, and Cu–Se atoms form a carrier conductive bond network that determines electrical conductivity. Therefore, it is possible to control the TE properties of  $\text{Cu}_2\text{SnSe}_3$  by doping on the Sn site. This can increase the effective mass to achieve a high Seebeck coefficient while preserving the 3D conductive framework as an electron-crystal like structure.<sup>7</sup> Reports have been published on the control of TE properties of  $\text{Cu}_2\text{SnSe}_3$  by substitution, doping and solid solution.<sup>8,9</sup> The dimensionless figure of merit ( $ZT$ ) of  $\sim 1.2$  was reported by Li *et al.* in an In-doped  $\text{Cu}_2\text{SnSe}_3$  compound at 850 K.<sup>10</sup>

Previous studies reported that  $\text{Cu}_2\text{SnSe}_3$  can be found in various allotropic forms, which include orthorhombic, monoclinic and cubic structures.<sup>11,12</sup> Phase transformation in solid-state compounds involves rearrangement of atoms, which can

<sup>a</sup> Department of Materials Science and Engineering, Seoul National University, Seoul 08826, Republic of Korea. E-mail: pchan@snu.ac.kr

<sup>b</sup> School of Chemical and Material Engineering, NUST, H-12, Islamabad, Pakistan

<sup>c</sup> Department of Nano Science and Engineering, Kyungnam University, Changwon, 51767, Republic of Korea

<sup>d</sup> Research Institute of Advanced Materials, Seoul National University, Seoul 08826, Republic of Korea

† Electronic supplementary information (ESI) available. See DOI: 10.1039/c7tc05180h

be induced by the change of temperature, pressure and/or composition. It is important to understand the thermodynamic conditions of these diverse phases since different synthesis conditions and stoichiometry can lead to the formation of different phases. Phase transitions can lead to different band gap and lattice parameters, which can further affect the physical properties.

The type of phases present at specific temperatures is controversial for  $\text{Cu}_2\text{SnSe}_3$ , due to the disagreements found in previous reports. Studies of Palantnik *et al.*<sup>13</sup> and Sharma *et al.*<sup>14</sup> reported that this compound crystallizes in a sphalerite-type cubic structure with the unit cell parameter ranging from  $a = 5.688$  to  $5.696$  Å. Debye–Scherrer powder analyses by Rivet *et al.*<sup>15</sup> indicated that  $\text{Cu}_2\text{SnSe}_3$  has an orthorhombic structure at  $450$  °C. On the other hand, XRD analyses by Marcano *et al.*<sup>16</sup> proposed a monoclinic structure for  $\text{Cu}_2\text{SnSe}_3$  with lattice parameters  $a = 6.5936$  Å,  $b = 12.1593$  Å,  $c = 6.6084$  Å and  $\beta = 108.56$  Å. Different compositions and synthesis parameters can lead to diverse results. Previous reports are lacking in providing specific composition, temperature and detailed TE characterization of  $\text{Cu}_2\text{SnSe}_3$  phases. Recently Fan *et al.*<sup>17</sup> used single crystal electron diffraction and high resolution synchrotron X-ray powder diffraction with Rietveld refinement to study the different crystal structures of  $\text{Cu}_2\text{SnSe}_3$ . Fan *et al.* further studied the structure of  $\text{Cu}_2\text{SnSe}_3$  samples water quenched from  $850$  K and  $950$  K, and found that they have monoclinic and cubic phase structures, respectively, but phase studies at temperatures lower than  $800$  K were not carried out. Further, the TE properties of the monoclinic phase  $\text{Cu}_2\text{SnSe}_3$  were studied, but those of the high temperature cubic phase have not been reported.

In this work, we performed phase studies using XRD on  $\text{Cu}_2\text{SnSe}_3$  samples solidified from the melt at  $1280$  K, annealed at different temperatures and subsequently water quenched. Rietveld refinements were used to obtain the quantitative phase information. Differentiation of the different phase structures was further confirmed by Raman spectroscopy analyses, and the TE properties of both the high and low temperature phases were compared in the temperature range of  $300$ – $600$  K.

## Experimental procedure

### (a) Sample preparation

A polycrystalline  $\text{Cu}_2\text{SnSe}_3$  sample was synthesized from direct reaction of stoichiometric amounts of Cu 99.99%, Sn 99.99%, and Se 99.99% powders (Kunjunodo Chemicals, Japan). The as-received powders were melted in a pre-evacuated quartz ampoule at  $1280$  K for 3 hours followed by periodic agitation to improve mixing of the reacting species. The molten sample was cooled at a rate of  $1$  K  $\text{min}^{-1}$  down to  $720$  K and  $820$  K, annealed for 12 hours at these temperatures and quenched in water to cease further phase changes.

In order to study phase transformation at higher temperatures, a molten sample was cooled to  $960$  K, annealed for 12 hours and quenched in water. The ingots were ground to a fine powder using an agate mortar-pestle, and the obtained powder samples were named hereafter M-720, M-820 and C-960 respectively. The powder

samples were spark-plasma-sintered (SPSed) at  $673$  K under the applied pressure of  $60$  MPa for 5 minutes. SPSed samples from M-720, M-820 and C-960 powders were named SM-720, SM-820 and SC-960, respectively. The consolidated samples were disc-shape pellets of  $3$  mm in height with  $12.5$  mm diameter.

### (b) Characterization

Phase studies were performed on the pellet samples using powder X-ray diffraction (XRD) with a D-8 Advance (Bruker, Germany), with copper  $K\alpha$  radiation of  $\lambda = 1.54$  Å. Rietveld refinement (TOPAS) was used for the quantitative phase analyses of the samples. The atomic displacement, fractional coordinates and occupancies of the elements, which were obtained from the standard XRD database, were used without refining. Raman scattering analyses were performed on the pellet samples using a LabRAM Raman spectrometer (HORIBA Scientific). The He–Ne laser source with a wavelength of  $532$  nm was used as the exciting light. The LabRAM spectrometer is equipped with both macro-analysis and microanalysis configurations. The laser beam of millimeter order spot size was focused on the sample surface using an optical input focusing macroanalysis system. The incident laser beam was further focused to  $1$   $\mu\text{m}$  spot size using an optical microscope ( $50\times$  objective) in the microanalysis system. All the measurements were performed in the range of  $50$ – $400$  ( $\text{cm}^{-1}$ ) Raman shift at ambient temperature.

The Seebeck coefficient and the electrical resistivity were measured in the temperature range of  $300$ – $600$  K using a commercial TE property measurement system (SEEPPEL, TEP-800). The measurements were carried out under an Ar atmosphere to prevent the oxidation of the SPSed samples.

A laser flash technique (LFA, Netzsch, LFA 457) was used to measure the thermal diffusivity ( $D$ ) of the carbon coated disc-shape samples with thickness  $<1$  mm in the temperature range of  $300$ – $600$  K under an inert atmosphere. Differential scanning calorimetry (DSC) was used to measure the specific heat ( $C_p$ ) in the same temperature range as  $D$ . The samples were put in an alumina crucible under an Ar atmosphere, and the DSC curve was recorded with a heating rate of  $10$  K  $\text{min}^{-1}$ . Thermal conductivity ( $k$ ) was calculated from  $k = C_p \cdot d \cdot D$ , where  $C_p$ ,  $d$  and  $D$  are the specific heat obtained from DSC, density and thermal diffusivity, respectively. The densities of the pellet samples were measured using Archimedes' principle at room temperature in ethanol medium. Hall effect measurements of carrier concentration ( $p_H$ ) and mobility ( $\mu_H$ ) on square-shape samples with thickness  $<1$  mm, were performed in van der Pauw configuration at room temperature with a  $0.56$  T applied magnetic field.

Ultraviolet-visible (UV-Vis) spectroscopy analyses were performed on the polycrystalline powder samples, dispersed in ethanol, using a UV-Vis/NIR spectrometer (JASCO, V-770). The optical absorption spectra were obtained in the wavelength range of  $600$ – $1000$  nm, with a step size of  $0.5$  nm.

DOS analyses and electronic band structure calculations were carried out for the SM-820 and SC-960 samples using the atomic positions and lattice parameters obtained from the Rietveld analysis of each sample. We performed first principles

calculations using the Vienna ab initio simulation package (VASP) based on the density functional theory (DFT).<sup>18</sup> The hybrid functional method based on HSE06<sup>19</sup> was employed for the exchange–correlation energy because of the band-gap underestimation in the conventional GGA scheme.<sup>20</sup> The fraction of exact exchange energy that we used was 0.25. The cut-off energy for the plane wave basis was set to 250 eV. In the crystal structure of cubic  $\text{Cu}_2\text{SnSe}_3$ , Cu and Sn atoms randomly occupy the same crystallographic site. To examine the influence of the site disorder on the electronic structure, we simulated three configurations where the Cu and Sn sites are distributed differently.

## Results and discussion

### (a) Phase analysis

The X-ray diffraction (XRD) patterns of the  $\text{Cu}_2\text{SnSe}_3$  powder samples annealed at 720 K (M-720), 820 K (M-820) and 960 K (C-960) and those of samples SPSed at 670 K for 5 minutes (SM-720, SM-820 and SC-960) are shown in Fig. S1 (ESI<sup>†</sup>) and Fig. 1(a), respectively. Fig. 1(b) shows the log scale XRD patterns of the SPSed samples in the range of 28–43 degree  $2\theta$ . Fig. S1 (ESI<sup>†</sup>) and Fig. 1(a) show that the XRD spectra remain the same before and after SPS sintering, hence the phases of the  $\text{Cu}_2\text{SnSe}_3$  samples were not affected by the SPS process. The XRD pattern in Fig. 1(a) shows that the  $\text{Cu}_2\text{SnSe}_3$  sample annealed at 960 K crystallizes in a cubic sphalerite type structure, represented by only the major peaks at 27.1, 45.0, 53.3 and 65.6 degrees  $2\theta$ . The low intensity peak of SC-960 shown in Fig. 1(b) around 30 degree  $2\theta$  is attributed to the minor monoclinic phase, formed during water quenching. The other two samples, annealed at 820 and 720 K, are found to have mostly monoclinic structures. Since these  $\text{Cu}_2\text{SnSe}_3$  allotropes are derived from the cubic sphalerite structure,<sup>21</sup> the XRD peaks with high intensities for all these phases are almost the same. The monoclinic phase of  $\text{Cu}_2\text{SnSe}_3$  can be distinguished from the cubic phase by the presence of

several peaks with very low intensities mostly between 28 and 43 degrees  $2\theta$  (Fig. 1(a)).

These experimental XRD spectra were analyzed further by Reitveld refinement using TOPAS to quantitatively distinguish the minor phases that can exist along with the parent phase. The results are shown in Fig. 2. The atomic positions, occupancies and thermal parameters of the PDF cards 04-002-6015 and 04-012-4693 for cubic and monoclinic structures, respectively, were used as an initial model for the refinement. The weighted pattern  $R$ -value ( $R_{\text{wp}}$ ) for all the samples was  $\sim 10$ , which we think is acceptable, with major peaks overlapping for different allotropic forms of  $\text{Cu}_2\text{SnSe}_3$ .

We found that it is very difficult to synthesize pure phase  $\text{Cu}_2\text{SnSe}_3$  at both low and high temperatures. The amount of cubic phase increases with increasing annealing temperature, and at high enough temperature, mostly cubic phase exists, which agrees well with the previous reports.<sup>11,17</sup> The samples annealed at 720 and 820 K consist of a major monoclinic phase with a minor cubic phase (2–11%) still present. This means that either the annealing time was not long enough to complete the high to low temperature phase transition or some local difference in composition of  $\text{Cu}_2\text{SnSe}_3$  crystallites lead to different phases. Similarly, the major phase of the sample annealed at high temperature (960 K) was cubic.

Fig. 3 shows the crystal structures of both the (a) monoclinic and (b) cubic phases of  $\text{Cu}_2\text{SnSe}_3$ . The monoclinic phase is a low temperature, less symmetric and ordered structure of  $\text{Cu}_2\text{SnSe}_3$ , where all the atoms are tetrahedrally coordinated. Sn and Cu bonded with four Se atoms form a three dimensional (Cu/Sn)– $\text{Se}_4$  corner shared 3D network. Se atoms are coordinated by one Sn and three Cu atoms, with bond lengths of Sn–Se  $\sim 2.60$  Å and Cu–Se  $\sim 2.44$  Å, as shown in Fig. 3(a). Cu and Sn are disordered in the cubic structure with a variety of possible cation coordination patterns around the Se anion like  $\text{Cu}_4$ ,  $\text{Cu}_3\text{Sn}$ ,  $\text{Cu}_2\text{Sn}_2$ ,  $\text{CuSn}_3$ , and  $\text{Sn}_4$ .<sup>22</sup>

We assumed an order–disorder transition for these allotropic transformations, where slight lattice re-arrangement can result in small atomic displacement from monoclinic (space group

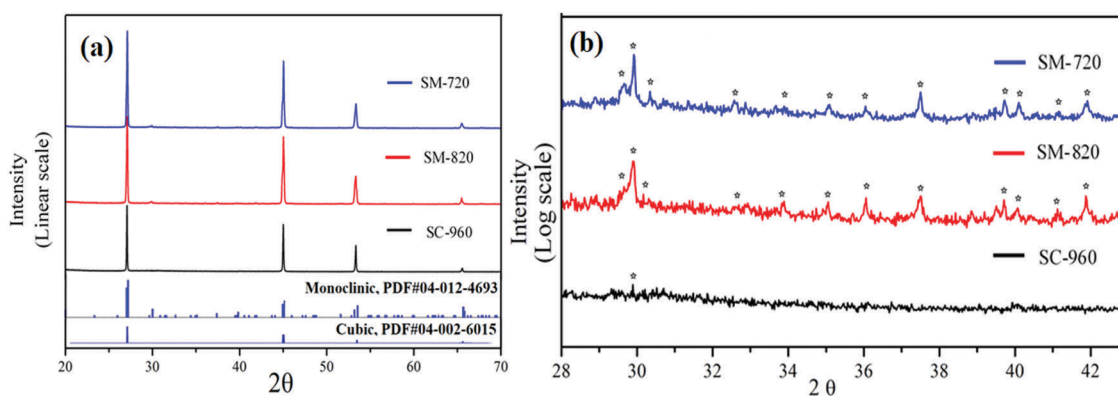


**Fig. 1** (a) XRD patterns of  $\text{Cu}_2\text{SnSe}_3$  powder samples annealed at 720 K (SM-720), 820 K (SM-820) and 960 K (SC-960) after melting in an evacuated quartz ampoule followed by water quenching. S means the samples were spark-plasma-sintered at 670 K for 5 minutes, M refers to the mostly monoclinic phase while C refers to the mostly cubic phase  $\text{Cu}_2\text{SnSe}_3$ . The bottom two lines represent the reference spectra (PDF card) of the cubic and monoclinic phases of  $\text{Cu}_2\text{SnSe}_3$ . (b) Log scale XRD patterns of the spark-plasma-sintered samples SM-720, SM-820 and SC-960 in the range of 28 to 43  $2\theta$  degrees show peaks (\*) that come from the monoclinic phase. The small peak around 30 degree  $2\theta$  in SC-960 reveals the presence of the minor monoclinic phase formed during quenching.

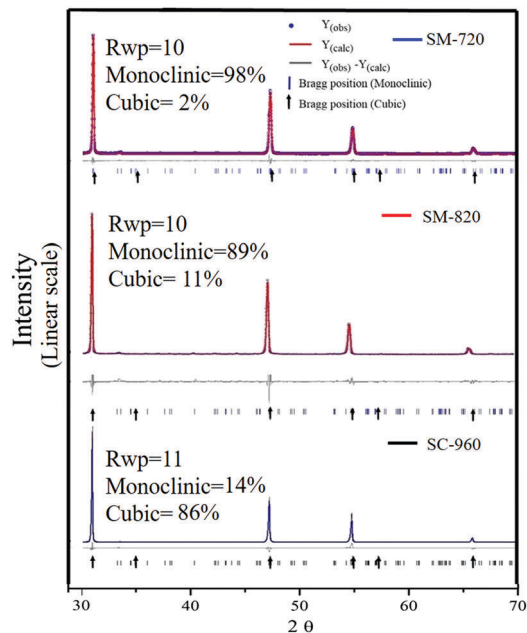


Fig. 2 Results of the Rietveld refinement quantitative phase analyses of SM-720, SM-820 and SC-960 samples are shown along with  $R_{wp}$  values in the upper left corner of each pattern. The dotted line is the original pattern; the solid line along the dotted line is the calculated one; the grey line shows the difference between calculated and observed patterns; and the dashed dots and arrows show the Bragg peak positions of the corresponding monoclinic and cubic phases.

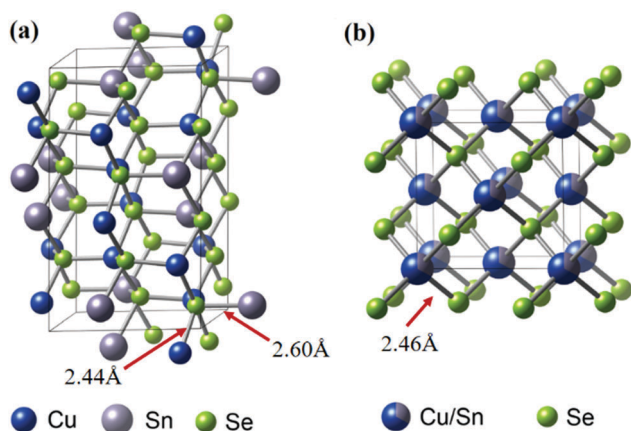


Fig. 3 Structure of (a) monoclinic and (b) cubic  $\text{Cu}_2\text{SnSe}_3$ , simulated from the Rietveld data files of the two samples.<sup>46</sup> The arrows show the bond lengths between the corresponding atoms. The bond length between Cu and Se is slightly larger for the monoclinic phase than that of the cubic structure. The mixed site occupancy of the Cu and Sn atoms is indicated by partial colouring of the corresponding atoms in (b).

9(Cc)) to cubic (space group  $216(F4\bar{3}m)$ ) at high temperature. In such types of phase transitions of  $\text{Cu}_2\text{SnSe}_3$ , the cubic to monoclinic transition is characterized by the presence of low intensity peaks in the XRD pattern, while the major reflections of (111), (022), (133) and (044) do not significantly change.<sup>23,24</sup>

Raman spectroscopy analyses were performed on the SM-820 and SC-960 samples in order to further confirm the monoclinic

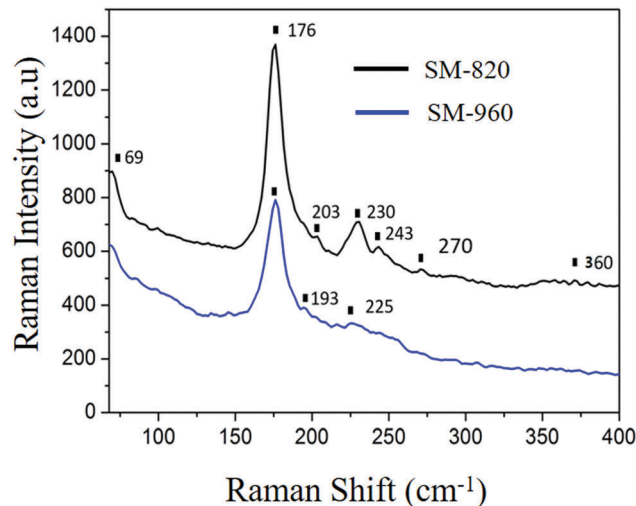


Fig. 4 Raman peaks of SC-960 and SM-820  $\text{Cu}_2\text{SnSe}_3$  powder samples obtained at room temperature, in the range of 40–400  $\text{cm}^{-1}$ . The Raman study was performed on the mostly cubic (SC-960) and mostly monoclinic (SM-820) phases.

to cubic phase transition at high temperature. The Raman spectra of the two samples, recorded in the range of 40–400  $\text{cm}^{-1}$ , are shown in Fig. 4. Raman shifts of the two samples in the present work are compared with those reported in the literature, and the results are listed in Table 1, where the possible symmetries are also assigned. Kroumov *et al.*<sup>25</sup> performed factor group analysis for the various zone-center lattice vibrational modes of the monoclinic  $\text{Cu}_2\text{SnSe}_3$  structure, with 3 Se, 1 Sn and 2 Cu atoms in 4(a) Wyckoff positions,<sup>26</sup> and argued that six Raman active modes, represented by  $3A' + 3A''$ , are possible for this compound (Table 1). The data obtained from the Raman peaks of the monoclinic structure agree well with both the calculated symmetry modes as well as those from the literature, indicated by six Raman shifts observed at 69, 176, 203, 230, 243 and 270  $\text{cm}^{-1}$ . The high intensity peak, observed at 176  $\text{cm}^{-1}$  in all the  $\text{Cu}_2\text{SnSe}_3$  phases, is attributed to the strongest  $A'$  mode, which resulted from the vibration of the Se–Cu bond, while Sn remains at rest. A broad vibrational band at  $\sim 360 \text{ cm}^{-1}$  was reported<sup>27</sup> as an overtone of the strong peak at 176  $\text{cm}^{-1}$ . In the high temperature cubic phase, only one intensive peak shift at 176  $\text{cm}^{-1}$  and two small intensity peaks at 193 and 225  $\text{cm}^{-1}$  are observed. The absence of the peaks at 203, 230 and 243  $\text{cm}^{-1}$  in the cubic phase confirms the phase transition, where these modes of lattice vibrations are lost in Raman scattering due to the increase in structural symmetry.<sup>28</sup>

In the cubic phase, the bond stretching force is small compared to the monoclinic ordered phase, due to the smaller bond length of Sn–Se in the cubic phase, as shown in Fig. 3. This can lead to a decrease in Raman shift due to a slight reduction in phonon energies, which was illustrated by Marcano *et al.*<sup>21</sup> The slight peak shifting towards lower Raman frequencies of  $\sim 10 \text{ cm}^{-1}$  for the cubic structure is in agreement with the fact that the high temperature phase of  $\text{Cu}_2\text{SnSe}_3$  has a disordered and more symmetric lattice structure. Finally, the major Raman

Table 1 Raman peak positions of SM-820 and SC-950 taken from Fig. 4 and compared with results from reported data

Raman peak (cm <sup>-1</sup> )								Symmetry assignments ref. 26
Peak no	Monoclinic			Cubic			(Calculated) (monoclinic) ref. 26	
	Present work	Ref. 26	Ref. 27	Present work	Ref. 28	Ref. 29		
1	69	83	75				82	A'
2	176	178	182	176	177	179	177	A'
3	203	204	196	193	203	199	Not calculated	A''
4	230	231	235	225	230	233	Not calculated	A''
5	243	244	251			250	246	A'
6	270	291					Not calculated	A''
7	360	363	366				356	A' + A' (overtone)

peak at 176 cm<sup>-1</sup> is the same for both Cu<sub>2</sub>SnSe<sub>3</sub> phases, which can be attributed to the Cu–Se bond vibration, since bond length is almost the same (~2.44 and 2.46 Å) in both compounds. From the XRD and Raman spectroscopy measurements, we conclude that Cu<sub>2</sub>SnSe<sub>3</sub> can be found in monoclinic structure as a major phase at a temperature of 820 K and below, while it has mostly cubic disordered structure at higher temperatures. Secondary phases like orthorhombic and tetragonal phases were not observed in this study.

### (b) Electronic transport properties

Annealing at high temperature can cause a phase transition and result in various electronic structures, since band gap is reduced with the increase in annealing temperature, which can be characterized by UV-Vis spectroscopy analysis. The dependence of energy band gap ( $E_g$ ) on the absorption coefficient ( $\alpha$ ) for the direct band transition is given by the relation<sup>29</sup>

$$\alpha h\nu = A(h\nu - E_g)^{1/2} \quad (1)$$

where  $A$ ,  $h$  and  $\nu$  are a constant, the Planck's constant and the frequency of radiation, respectively. Fig. S2 (ESI<sup>†</sup>) shows the optical absorption spectra obtained from the UV-Vis spectroscopy for the SM-820 and SC-960 powder samples dispersed in ethanol at room temperature. The calculated values of  $h\nu$  and  $(\alpha h\nu)^2$  are plotted in Fig. 5 for the (a) monoclinic and (b) cubic structures. The optical band gaps were obtained from the extrapolation of the linear region of the plot to the  $h\nu$  axis, and were found to be 0.9 eV and 1.0 eV for the monoclinic and cubic phase, respectively. The values of the direct band gaps of Cu<sub>2</sub>SnSe<sub>3</sub> reported previously lie in the range of 0.3–1.3 eV,<sup>16,30,31</sup> which is in agreement with the results in this study.

To further study the changes in band structure accompanying the phase transition, we studied the density of states (DOS) and band structures of the samples SM-820 and SC-960. The structure information of the major phase from the Rietveld refinement of the samples SM-820 and SC-960 was used for the calculation. Fig. 6(a) and 7(a) show the band structures of the monoclinic and cubic phases. In the monoclinic phase, the conduction band (CB) minima and the valence band (VB) maxima are separated clearly at the point  $\Gamma$ . The band gap of 0.58 eV is consistent with the experimental observation. On the contrary, in the cubic structure, the metallic band structure is observed. The change of band gap according to the phase

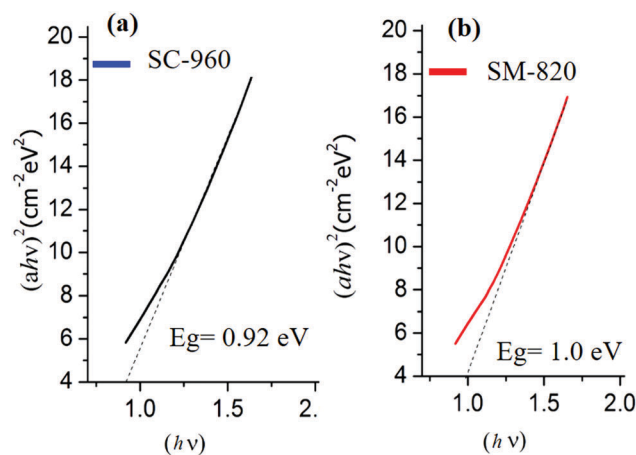


Fig. 5 UV-Vis spectroscopy measurements for the SM-820 and SC-960 powder samples. The calculated values of  $h\nu$  and  $[(\alpha h\nu)]^2$  are plotted for the (a) monoclinic and (b) cubic phases. The band gap value for each phase was obtained by extrapolating these plots to the  $X$ -axis.

transition has been reported for other phase variant structures like MTe<sub>2</sub> (M = Mo and W)<sup>32</sup> and ZnS.<sup>33</sup> Fig. 6(b) and 7(b) show that the VB maximum is mainly contributed by Se-p and Cu-d orbital hybridization in the VB, while the major part of the CB minimum is occupied by Sn-s and Se-p hybridized orbitals. The orbital character of the VB indicates that the Cu–Se bonding network plays the dominant role in the hole transport of the p-type Cu<sub>2</sub>SnSe<sub>3</sub>. On the other hand, Sn atoms do not contribute to the hole conduction but provide extra electrons to the whole lattice.<sup>7</sup>

Fig. S3 (ESI<sup>†</sup>) shows the (a) hole concentration and (b) carrier mobility of SM-820 (square points) and SC-960 (circle points) measured at room temperature. The DFT results are also consistent with the results in Fig. S2 (ESI<sup>†</sup>), where the carrier concentration in the cubic phase is higher than that of the monoclinic phase. The variation in the band gap ( $E_g$ ) of heavily doped semiconductors like Cu<sub>2</sub>SnSe<sub>3</sub> can be governed by the Burstein–Moss effect,<sup>34</sup> where the conduction band comes closer to the Fermi energy level ( $E_F$ ), due to the increase in carrier concentration.

The relation between the carrier concentration and band gap is given as<sup>35</sup>

$$n_i = CT^{3/2} \exp\left(\frac{-E_g}{2k_B T}\right) \quad (2)$$

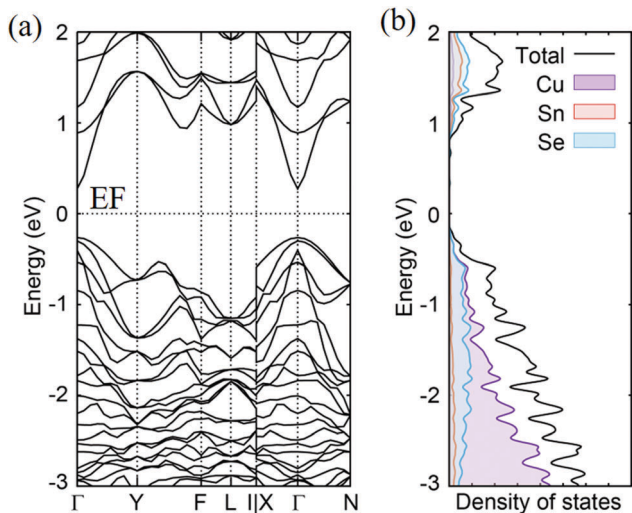


Fig. 6 (a) Band structure and (b) projective density of states of the sample SM-820 obtained by first-principles calculations.  $E_F$  is the Fermi energy level of the system. The spacing between conduction band minimum and valence band maximum at the zero symmetry point  $\Gamma$  is the electronic band gap.

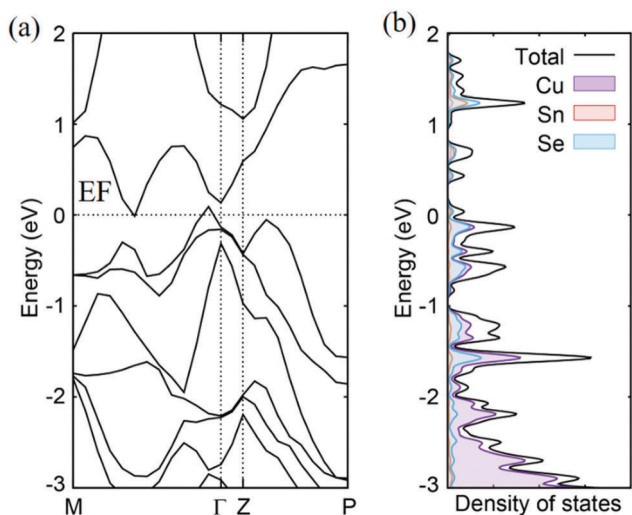


Fig. 7 (a) Band structure and (b) projective density of states of the sample SC-960 obtained by first-principles calculations.  $E_F$  is the Fermi energy level of the system. There is no band gap at the  $E_F$ .

where  $C$ ,  $T$ ,  $k_B$ ,  $n_i$  and  $E_g$  are a constant, the absolute temperature, the Boltzmann constant, the carrier concentration and the band gap, respectively. The carrier concentration is exponentially proportional to the negative of the band gap, which means that band gap narrowing leads to the increase of the carrier concentration. Thus, the band gap reduction of the cubic phase compared to the monoclinic phase can result in the major increase of carrier concentration.

Moreover, electrical conductivities of both  $\text{Cu}_2\text{SnSe}_3$  phases are reduced with increasing temperature, which is a common behavior for heavily doped degenerate semiconductors.<sup>36</sup> Here, the Se loss resulting from the high temperature treatment can lead to the increase of the hole concentration, which in turn,

can increase the electrical conductivity. These results are in good agreement with the results of band gap analyses and the hall measurements discussed above.

### (c) Thermoelectric properties

Fig. 8 shows the TE properties measured in the temperature range of 300 K–600 K. The Seebeck coefficients of both the monoclinic and cubic phase have a linear relationship with temperature, which validates the degenerate behavior shown in Fig. 8(b). The Seebeck coefficients of the monoclinic phase, which are larger than those of the cubic  $\text{Cu}_2\text{SnSe}_3$  phase, can be explained using the mobility of majority carriers. Sun *et al.*<sup>37</sup> studied the effect of mobility, charge relaxation ( $t$ ) and carrier potential on the Seebeck coefficient, where they included the effect of asymmetric charge relaxation ( $S_t$ ) in the Mott expression. The expression describes the Seebeck coefficient in the form of two factors,  $S_t$  (asymmetric charge relaxation) and  $S_N$  (conventional contribution),

$$S = S_t + S_N = -\frac{\pi^2 k_B^2 T}{3} \frac{1}{2} \left[ \frac{\partial \ln \tau}{\partial \varepsilon} \right]_{\varepsilon_F} - \frac{\pi^2 k_B^2 T}{3} \frac{1}{2} \left[ \frac{\partial \ln N}{\partial \varepsilon} \right]_{\varepsilon_F}, \quad (3)$$

$S_t$  can be further related to the Nernst coefficient,

$$\nu = -\frac{\pi^2 k_B^2 T}{3} \frac{1}{B|e|} \left[ \frac{\partial \tan \theta_H}{\partial \varepsilon} \right]_{\varepsilon_F}, \quad (4)$$

by  $\nu \cdot B = \pm S_t \tan \theta_H$ , where  $\varepsilon$  is energy function,  $\varepsilon_F$  is the Fermi level,  $\tan \theta_H$  is the tangent of the Hall angle and  $B$  is the magnetic field. The Nernst coefficient weakly depends on ordinary scattering processes, but has a pronounced dependency on charge relaxation events.  $\nu$  can be further expressed in terms of either charge mobility  $\mu$  or  $\tau$ , since  $\tan \theta_H = eB\tau/m^* = \mu B$ . We assume that the effect of  $S_N$  on the Seebeck coefficient is not prominent, as the stoichiometric composition of the samples used in this study is supposed to be unchanged and only the structures are slightly varied. Fig. S3(b) (ESI<sup>†</sup>) shows that the carrier mobility of the monoclinic phase at room temperature is higher than that of the cubic phase. This enhanced mobility in the ordered structure can be related to the carrier concentration, which is smaller than that of the disordered structure, and was already discussed in the electronic structure study. From the Nernst and charge relaxation expressions, it can be apparently seen that the Seebeck coefficient has a direct physical link with the charge mobility, while the Seebeck coefficient is further increased with increasing temperature. Moreover, the Seebeck coefficient measured at 600 K in this study is smaller than  $100 \mu\text{V K}^{-1}$  for both SM-820 and SC-960 samples, which is lower than the recently reported  $120 \mu\text{V K}^{-1}$  by Li, *et al.*<sup>10</sup> and  $200 \mu\text{V K}^{-1}$  by Liu, *et al.*<sup>38</sup> High carrier concentration can lead to large carrier scattering, which can result in the decrease of carrier mobility and Seebeck coefficient.

The dimensionless figure of merit ( $ZT$ ), calculated from electrical conductivity, Seebeck coefficient and thermal conductivity are given in Fig. 8(d).  $ZT$  values for both phases (SM-820 and SC-960) show a linear increase with temperature. The sample SC-960 (mostly cubic phase) shows a  $ZT$  of 0.09 at 600 K, which is comparable

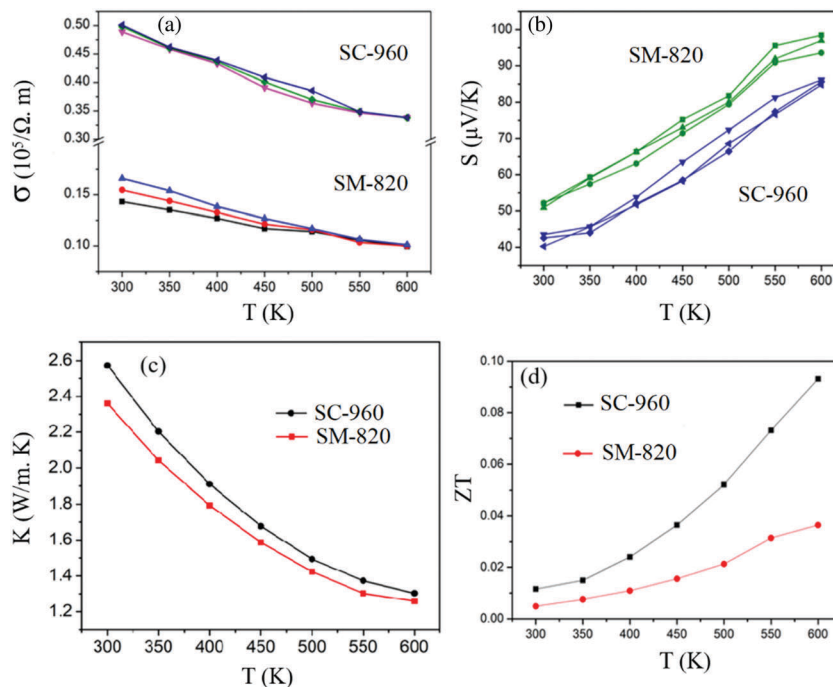


Fig. 8 Temperature dependence of (a) electrical conductivity, (b) Seebeck coefficient, (c) thermal conductivity, and (d) thermoelectric figure of merit  $ZT$  for the spark-plasma-sintered samples SM-820 and SC-960. Electrical conductivity and Seebeck coefficient measurements were recorded three times to ensure the reproducibility of results.

with the recently reported value ( $\sim 0.1$ ) for the undoped  $\text{Cu}_2\text{SnSe}_3$ .<sup>10</sup> The TE performance of cubic  $\text{Cu}_2\text{SnSe}_3$ , which is higher than that of the monoclinic phase, can be attributed to the increase in electrical conductivity due to the reduction of the band gap. The contributions of both the thermal conductivity and the Seebeck coefficient to the  $ZT$  in the cubic phase are not large enough to synergistically balance the increase in electrical conductivity. Hence, the power factor of the cubic phase ( $0.24 \text{ mW m}^{-1} \text{ K}^{-2}$ ) was higher than that of the monoclinic phase ( $0.096 \text{ mW m}^{-1} \text{ K}^{-2}$ ) at 600 K, but the change of thermal conductivity was not significant.

The thermal conductivity results are shown in Fig. 8(c), where both phases have nearly the same values, which decreased with temperature in a similar way. To find the reason for the large difference in electrical conductivity and similar thermal conductivity of the monoclinic and cubic phases, we split the whole thermal conductivity into the electronic part ( $K_e$ ) and the lattice part ( $K_l$ ). The Wiedemann–Franz law<sup>39</sup> ( $K_e = L\sigma T$ , where  $L$  is the Lorenz number) was employed to determine  $K_e$  in the temperature range of 300–600 K. In the above relationship, it is crucial to determine the value of  $L$  before going into further calculations.

Typically, for the metallic elements, the free-electron model<sup>40</sup> is employed, using:

$$L_0 = \frac{\pi^2}{3} \left( \frac{k_B}{e} \right)^2, \quad (5)$$

where  $k_B$  is the Boltzmann constant and  $e$  is the charge of electron. The  $L_0$  value obtained from eqn (5) is  $\sim 2.45 \times 10^{-8} \text{ W } \Omega \text{ K}^{-2}$ , which is used to calculate  $K_e$  for the metals. However, for heavily doped degenerate semiconductors like  $\text{Cu}_2\text{SnSe}_3$ , chemical potential is strongly dependent on the temperature, hence the Lorenz

number does not remain the same for the whole temperature range. Using the single value of the Lorenz number would underestimate the lattice thermal conductivity. The true value of  $L$  depends on the reduced Fermi energy  $\eta$  ( $= E_F/k_B T$ ) and the acoustic phonon scattering parameter  $\lambda$ . The corresponding equation for calculating  $L$  is:<sup>41</sup>

$$L = \left( \frac{k_B}{e} \right)^2 \frac{(1 + \lambda)(3 + \lambda)F_{\lambda}(\eta)F_{\lambda+2}(\eta) - (2 + \lambda)^2 F(\eta)_{\lambda+1}^2}{(1 + \lambda)^2 F(\eta)_{\lambda}^2}, \quad (6)$$

where  $\lambda = 0$  for the acoustic phonon scattering. The fermi integrals ( $F_m(\eta)$ ) were measured from the experimental Seebeck coefficients, using the simple parabolic band model:

$$S = \left( \frac{k_B}{e} \right) \left( \frac{2F_1(\eta)}{F_0(\eta)} - \eta \right) \quad (7)$$

The detailed calculation procedure can be found in the literature.<sup>41,42</sup> The calculated Lorenz numbers are shown in Fig. S4(a) (ESI<sup>†</sup>). Using these  $L$  values, we calculated the corresponding electronic part of thermal conductivity and then subtracted it from the total thermal conductivity to get the lattice thermal conductivity for each of the samples, which is shown in Fig. S4(b) and (c) (ESI<sup>†</sup>).

It can be seen from Fig. S4 (ESI<sup>†</sup>) that the electronic conductivities are very different, while the lattice parts of the thermal conductivities are nearly the same for the samples SM-820 and SC-960. This means that the lattice vibration has a negligible role in the increase of total thermal conductivity of SM-820, since the major effect comes from the different electronic

thermal conductivities. Further, the lower lattice thermal conductivity of SC-960 in Fig. S4(b) (ESI†) reveals that it has large phonon scattering due to the disordered lattice structure. The monoclinic to cubic phase transition results in the increase of crystal symmetry and disorder, which leads to the increase of phonon scattering of the cubic phase. Loss of crystal symmetry due to the order–disorder transition was reported by Richardson *et al.*,<sup>43</sup> while its effect on phonon scattering and thermal conductivity was recently explored.<sup>44,45</sup> The presence of the mixed phases in both samples provides an extra scattering factor to reduce the total thermal conductivity, which is favorable for a higher *ZT*.

## Conclusion

The effect of annealing temperature on the phase transition of  $\text{Cu}_2\text{SnSe}_3$  was investigated, and the TE properties of the monoclinic and cubic phases of  $\text{Cu}_2\text{SnSe}_3$  were compared for the first time. A stoichiometric composition of  $\text{Cu}_2\text{SnSe}_3$  was synthesized by melt solidification and heat treatment at various temperatures followed by water quenching. XRD analyses reveal that the samples annealed at 720 and 820 K have mostly a monoclinic phase along with a small amount of cubic phase.  $\text{Cu}_2\text{SnSe}_3$  annealed at 960 K is mostly cubic. In order to investigate the effect of phase transition on the TE performance of  $\text{Cu}_2\text{SnSe}_3$ , TE properties of the samples SPSeD at 673 K for 5 min using the powder annealed at 820 (SM820) and 960 (SC960) followed by water quenching were measured in the temperature range of 300–600 K. It was found that the mostly cubic phase SC-960 sample has a much higher *ZT* than the mostly monoclinic phase sample. The better TE performance of high temperature cubic phase SC-960 can be attributed to the smaller band gap ( $\sim 0.92$  eV), which can lead to higher electrical conductivity compared to monoclinic SM-820 ( $\sim 1.0$  eV) at room temperature.

Although the electrical conductivity of the cubic phase is enhanced due to the reduction in band gap and high carrier concentration, the increase of thermal conductivity is much smaller than that of the electrical conductivity. One possible reason for the relatively small increase of thermal conductivities of both the monoclinic and cubic phase is the presence of the minor secondary phase, which can promote the phonon scattering and reduce the thermal conductivity. The results show that the cubic phase  $\text{Cu}_2\text{SnSe}_3$  is a better candidate for TE applications than the monoclinic phase, because the cubic phase has better TE performance and the performance can be further improved by optimizing the Seebeck coefficient by doping at Sn sites or by interstitial alloying.

## Conflicts of interest

There are no conflicts to declare.

## Acknowledgements

This work was supported by the National Research Foundation of Korea (NRF) grant funded by the Ministry of Science, ICT & Future Planning (MSIP) (No. NRF-2015R1A5A1037627).

## References

- 1 Y. N. Xie, T. M. Chou, W. F. Yang, M. H. He, Y. R. Zhao, N. Li and Z. H. Lin, *Semicond. Sci. Technol.*, 2017, **32**, 044003.
- 2 N. Toshima, *Synth. Met.*, 2017, **225**, 3–21.
- 3 Q. Wu and J. L. Hu, *Smart Mater. Struct.*, 2017, **26**, 045037.
- 4 Y. Mao, Y. G. Yan, K. P. Wu, H. Y. Xie, Z. K. Xiu, J. H. Yang, Q. J. Zhang, C. Uher and X. F. Tang, *RSC Adv.*, 2017, **7**, 21439–21445.
- 5 S. N. Girard, J. He, X. Zhou, D. Shoemaker, C. M. Jaworski, C. Uher, V. P. Dravid, J. P. Heremans and M. G. Kanatzidis, *J. Am. Chem. Soc.*, 2011, **133**, 16588–16597.
- 6 L. Xi, Y. B. Zhang, X. Y. Shi, J. Yang, X. Shi, L. D. Chen, W. Zhang, J. H. Yang and D. J. Singh, *Phys. Rev. B: Condens. Matter Mater. Phys.*, 2012, **86**, 155201.
- 7 X. Y. Shi, L. L. Xi, J. Fan, W. Q. Zhang and L. D. Chen, *Chem. Mater.*, 2010, **22**, 6029–6031.
- 8 Y. Y. Li, G. H. Liu, J. T. Li, K. X. Chen, G. He, Z. C. Yang, Y. M. Han, M. Zhou and L. F. Li, *Mater. Chem. Phys.*, 2016, **177**, 398–404.
- 9 S. Singh, M. Brandon, P. Liu, F. Laffir, W. Redington and K. M. Ryan, *Chem. Mater.*, 2016, **28**, 5055–5062.
- 10 Y. Y. Li, G. H. Liu, T. F. Cao, L. M. Liu, J. T. Li, K. X. Chen, L. F. Li, Y. M. Han and M. Zhou, *Adv. Funct. Mater.*, 2016, **26**, 6025–6032.
- 11 J. Fan, H. L. Liu, X. Y. Shi, S. Q. Bai, X. Shi and L. D. Chen, *Acta Mater.*, 2013, **61**, 4297–4304.
- 12 J. Fan, W. Schnelle, I. Antonyshyn, I. Veremchuk, W. Carrillo-Cabrera, X. Shi, Y. Grin and L. D. Chen, *Dalton Trans.*, 2014, **43**, 16788–16794.
- 13 L. S. Palatnik, V. M. Koshkin, L. P. Galchinetskii, V. I. Kolesnikov and Y. F. Komnik, *Phys. Solid State*, 1962, **4**, 1052–1053.
- 14 B. B. Sharma, R. Ayyar and H. Singh, *Phys. Status Solidi A*, 1977, **40**, 691–696.
- 15 J. Rivet, *Ann. Chim.*, 1965, **10**, 243.
- 16 G. Marcano, C. Rincon, L. M. de Chalraud, D. B. Bracho and G. S. Perez, *J. Appl. Phys.*, 2001, **90**, 1847–1853.
- 17 J. Fan, W. Carrillo-Cabrera, L. Akselrud, I. Antonyshyn, L. D. Chen and Y. Grin, *Inorg. Chem.*, 2013, **52**, 11067–11074.
- 18 G. Kresse and J. Furthmüller, *Phys. Rev. B: Condens. Matter Mater. Phys.*, 1996, **54**, 11169–11186.
- 19 J. Heyd, G. E. Scuseria and M. Ernzerhof, *J. Chem. Phys.*, 2006, **124**, 219906.
- 20 S. Park, B. Lee, S. H. Jeon and S. Han, *Curr. Appl. Phys.*, 2011, **11**, S337–S340.
- 21 M. E. Norako, M. J. Greaney and R. L. Brutchey, *J. Am. Chem. Soc.*, 2012, **134**, 23–26.
- 22 J. J. Wang and K. M. Ryan, *CrystEngComm*, 2016, **18**, 3161–3169.
- 23 L. D. Gulay, M. Daszkiewicz, T. A. Ostapyuk, O. S. Klymovych and O. F. Zmiy, *Acta Crystallogr., Sect. C: Struct. Chem.*, 2010, **66**, 158–160.
- 24 Y. T. Zhai, S. Y. Chen, J. H. Yang, H. J. Xiang, X. G. Gong, A. Walsh, J. Kang and S. H. Wei, *Phys. Rev. B: Condens. Matter Mater. Phys.*, 2011, **84**, 075213.
- 25 E. Kroumova, M. I. Aroyo, J. M. Perez-Mato, A. Kirov, C. Capillas, S. Ivantchev and H. Wondratschek, *Phase Transitions*, 2003, **76**, 155–170.

- 26 G. E. Delgado, A. J. Mora, G. Marcano and C. Rincon, *Mater. Res. Bull.*, 2003, **38**, 1949–1955.
- 27 G. Marcano, C. Rincon, S. A. Lopez, G. S. Perez, J. L. Herrera-Perez, J. G. Mendoza-Alvarez and P. Rodriguez, *Solid State Commun.*, 2011, **151**, 84–86.
- 28 J. J. Wang, A. Singh, P. Liu, S. Singh, C. Coughlan, Y. N. Guo and K. M. Ryan, *J. Am. Chem. Soc.*, 2013, **135**, 7835–7838.
- 29 P. U. Bhaskar, G. S. Babu, Y. B. K. Kumar and V. S. Raja, *Appl. Surf. Sci.*, 2011, **257**, 8529–8534.
- 30 G. S. Babu, Y. B. K. Kumar, Y. B. K. Reddy and V. S. Raja, *Mater. Chem. Phys.*, 2006, **96**, 442–446.
- 31 D. H. Kuo, W. D. Haung, Y. S. Huang, J. D. Wu and Y. J. Lin, *Surf. Coat. Technol.*, 2010, **205**, S196–S200.
- 32 H. H. Huang, X. F. Fan, D. J. Singh, H. Chen, Q. Jiang and W. T. Zheng, *Phys. Chem. Chem. Phys.*, 2016, **18**, 4086–4094.
- 33 F. A. La Porta, L. Gracia, J. Andres, J. R. Sambrano, J. A. Varela and E. Longo, *J. Am. Ceram. Soc.*, 2014, **97**, 4011–4018.
- 34 E. Burstein, *Phys. Rev.*, 1954, **93**, 632–633.
- 35 J. Jimenez and J. W. Tomm, *Spectroscopic Analysis of Optoelectronic Semiconductors*, Springer, Switzerland, 2016, DOI: 10.1007/978-3-319-42349-4.
- 36 Y. W. Shen, C. Li, R. Huang, R. M. Tian, Y. Ye, L. Pan, K. Koumoto, R. Z. Zhang, C. L. Wan and Y. F. Wang, *Sci. Rep.*, 2016, **6**, 32501.
- 37 P. J. Sun, B. P. Wei, J. H. Zhang, J. M. Tomczak, A. M. Strydom, M. Sondergaard, B. B. Iversen and F. Steglich, *Nat. Commun.*, 2015, **6**, 7475.
- 38 G. H. Liu, K. X. Chen, J. T. Li, Y. Y. Li, M. Zhou and L. F. Li, *J. Eur. Ceram. Soc.*, 2016, **36**, 1407–1415.
- 39 D. M. Rowe, *Thermoelectrics handbook: macro to nano*, CRC/Taylor & Francis, Boca Raton, 2006.
- 40 K. Momma and F. Izumi, *J. Appl. Crystallogr.*, 2011, **44**, 1272–1276.
- 41 S. Johnsen, J. Q. He, J. Androulakis, V. P. Dravid, I. Todorov, D. Y. Chung and M. G. Kanatzidis, *J. Am. Chem. Soc.*, 2011, **133**, 3460–3470.
- 42 A. F. May, J. P. Fleurial and G. J. Snyder, *Phys. Rev. B: Condens. Matter Mater. Phys.*, 2008, **78**, 125205.
- 43 J. W. Richardson, D. L. Price and M. L. Saboungi, *Phys. Rev. Lett.*, 1996, **76**, 1852–1855.
- 44 P. S. Whitfield, N. Herron, W. E. Guise, K. Page, Y. Q. Cheng, I. Milas and M. K. Crawford, *Sci. Rep.*, 2016, **6**, 35685.
- 45 R. M. Murphy, E. D. Murray, S. Fahy and I. Savic, *Phys. Rev. B: Condens. Matter Mater. Phys.*, 2016, **93**, 104304.